Hydrodynamic Separation of Particles Using Pinched-Flow Fractionation

John F. Ashley, Christopher N. Bowman, and Robert H. Davis
Dept. of Chemical and Biological Engineering, University of Colorado, Boulder, CO 80309

DOI 10.1002/aic.14087
Published online March 26, 2013 in Wiley Online Library (wileyonlinelibrary.com)

Rigid particles transported through a pinched-flow fractionation (PFF) device are simulated using boundary-integral methods (BIM). The PFF device separates particles by size using a bifurcated microfluidic channel. The critical flow ratio of the two input channels required to achieve complete separation of large and small particles decreases with increasing diameter of the larger particles relative to the pinch height, and is nearly independent of the smaller particle size. A narrow pinch with a square exit was shown to have the lowest critical flow ratio and was selected as the model device to be fabricated. Experiments conducted using this device confirm that the larger particles exit further from the top wall than do the smaller particles, due to steric exclusion, and the final exit positions are within a few percent of the simulation results. It is shown that BIM is a valuable tool in the design of microfluidic devices. © 2013 American Institute of Chemical Engineers *AIChE J*, 59: 3444-3457, 2013
Keywords: complex fluids, computational fluid dynamics, microfluidics, particulate flows, separation techniques

Introduction

The use of microchannel devices to sort and separate particles in a liquid is important for many industries and applications. For example, biotechnology and biomedical industries use processes that separate viruses, cells, organelles, and microbes by size,[1–7] while various manufacturing applications require sorting of ceramic particles, polymeric beads, and components of encapsulated drug-delivery systems and use microchannel devices that separate particles by size.[8]

Several methods utilizing microchannel devices are available for microparticle separation. Dielectrophoresis (DEP)[9–11] and field-flow fractionation (FFF)[12–18] allow for the sorting of particulate matter on a limited scale using microfluidics. Continuous microparticle separation methods include continuous DEP, acoustic methods, and split-flow fractionation.[19,20]

In this work, particles made neutrally buoyant by suspension in a fluid of equal density are separated by size using pinched-flow fractionation (PFF). PFF, as illustrated in Figure 1, provides a method for separation of small particles by size based on principles of fluid mechanics and steric exclusion.[21] Incorporation of PFF in a microchip would provide for the continuous separation of particulate matter utilizing microfluidics. Figure 1 shows a pinched-flow-fractionation channel (not to scale), with key sections labeled. The device consists of two inlet or entry channels separated by an angle θ_i, a pinch area, and an expansion area that serves as an exit. It is assumed that channel width W in the direction normal to the plane of Figure 1 is large compared to the channel height H, so that the flow of pure fluid through the channel is two-dimensional (2-D). However, the introduction of particles into this device gives rise to three-dimensional (3-D) flow around the particles. Particles are introduced along with suspending fluid in the top inlet channel (subscript i), while pure fluid (without particles) is introduced in the bottom sweep channel (subscript s) to force the particles toward the upper wall of the pinch region (subscript p). At lower flow ratios, defined as the ratio Q_s/Q_i of the sweep and inlet flow rates, the particles are not all forced near the upper pinch wall and incomplete separation of particles in the exit area takes place, resulting in a "banding" effect. Under these circumstances, a "band" of exit trajectories forms for each particle size, with the potential for suboptimal conditions in which overlap of the bands occurs for particles of different sizes. At high flow ratios, all particles are essentially pressed against the upper wall of the pinch, such that all particles of a given size theoretically would follow a single trajectory into the exit region (subscript e), starting at one radius from the upper wall of the pinch. Thus, under these conditions, all larger particles remain a greater distance from the wall, follow a distinct trajectory exiting the pinch region, and ultimately can be separated from smaller particles.

PFF has previously been demonstrated in a microchannel device as a way to separate microparticles by size with continuous flow.[22] Targeted applications include size determination of air-borne particles,[23] marine-sediment measurement, and whole-blood separation.[24,25] Channel geometry, particle size, fluid transport, and volumetric flow ratio of input-channel fluids are all known to affect the trajectories of particle motion through the device. Andersen et al.[26] recently developed a model based on the laminar velocity profile in a

Correspondence concerning this article should be addressed to R. H. Davis at robert.davis@colorado.edu.

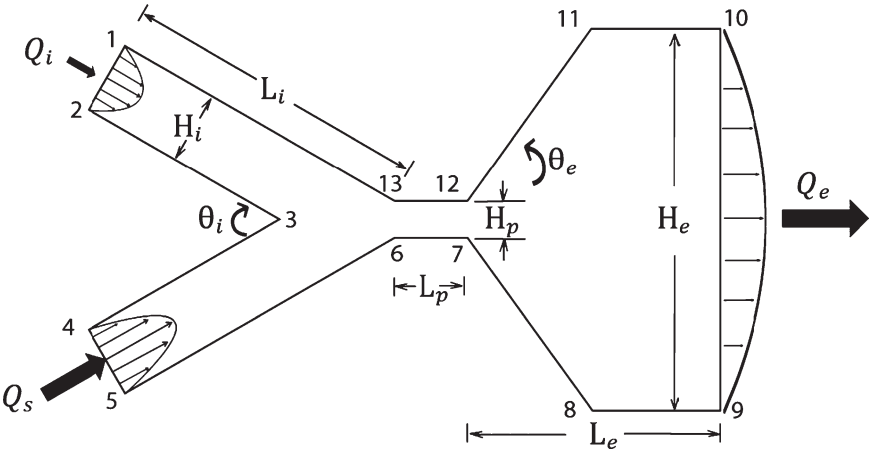

Figure 1. Idealized (not to scale) representation of a PFF device.

The schematic shows two inlet channels (left side), the pinch region (mid diagram), and the exit area (right side). Vertices are shown, and are numbered counter-clockwise starting from the upper-inlet channel. Inlet flow rates (Q_i, Q_s) and exit flux ($Q_e = Q_i + Q_s$) are illustrated to include Poiseuille flow profiles. The angle described by the bifurcation of the two input channels is noted by θ_i, while the exit angle from the pinch region is represented by θ_e. Dimensions of the device are represented by L_i (length of inlet channel), L_p (length of pinch area), L_e (length of exit channel), H_i (height of inlet channel), H_p (height of pinch area), and H_e (height of exit area).

rectangular channel[27] and assuming that particles leave the top corner of the pinch and follow the fluid streamlines into different exit or drain channels depending on particle size. This model provides better agreement with experiments than previous models. However, rather than simply understanding only the idealized separation behavior, it is important to determine the conditions under which particles actually reach the top of the pinch and the degree to which hydrodynamic interactions with the walls and corners affect the trajectories. Systematic studies of the hydrodynamic, particle-wall, and particle-corner interactions that produce the PFF effects have only recently been developed, using a moving-frame, boundary-integral method (BIM) to describe the particle trajectories.[28]

In the current work, the moving-frame BIM is used to simulate the trajectories of the particles as they are transported through the PFF device. The effects related to the distant walls perpendicular to the channel walls shown in Figure 1 are neglected, which is valid for large aspect ratios and allows for a reduction in the dimensionality of the calculations required to build a model. BIM has the advantage of further reducing the dimensionality of the model, as implementation only requires integration at the particle and device surfaces. Limiting the discretization to these surfaces reduces the computational requirements when compared to other methods such as finite-difference, volume-of-fluid, or finite-element methods. The ability to optimize application-specific operation based on information obtained from BIM simulations alleviates the need for fabricating multiple device configurations. We use this BIM to design a device with favorable separation characteristics, which was subsequently used to perform experiments that were compared with the model predictions.

Simulation Method

BIM formulation

Our approach uses a moving-frame, 3-D BIM developed for use in channels where the surfaces of particles and walls affecting particle movement are discretized. The boundary-integral equations are standard (e.g., Pozrikidis,[29] Ladyzhenskaya,[30] and Kim and Karilla.[31]). However, complex channel geometries, with the narrow channel dimensions being comparable to the particle size, but much smaller than the overall channel domain, present computational challenges for numerical simulations. To address these difficulties, a "moving-frame, BIM"[28] was developed, to provide a solution where the computational domain around the particle changes while a particle moves through the complex channel. The problem is formulated in terms of boundary-integrals for the surface potential, with the fluid velocity on the cell boundary taken from the 2-D solution for fluid-flow only, and solved iteratively at each time step. The method is outlined here, and the details are provided in Zinchenko et al.[28]

The moving-frame, BIM is systematically used to study the effects of particle radius, the ratio of flow rates, and the channel geometry on particle trajectories and the efficiency of size segregation. Using a two-step approach, a 2-D model of the fluid transport through the channel with no particles is first determined using BIM. A sphere is then placed within the fluid-only, 2-D flow field, and the trajectory of the sphere is determined using the 3-D, moving-frame BIM. Our BIM calculations are used to determine when there is a significant difference between particle trajectories and the fluid streamlines, and to predict the critical conditions for complete separation of particles of different sizes along with the degree of separation when operated under subcritical conditions. The approach is quite general for various microchannel geometries, consisting of an arbitrary number of rectangular panels, and is not limited to spherical particles.

For microfluidic applications with small Reynolds numbers, inertia may be neglected, so that creeping or Stokes flow may be assumed, which is a prerequisite for using a boundary-integral approach. The velocity $\boldsymbol{u}_\infty$ for fluid-only flow in the device channel is calculated first. Once determined, the velocity $\boldsymbol{u}_\infty$ serves as the outer boundary condition used to solve the 3-D problem, where particles are being transported in the fluid. The expression for the fluid-only velocity inside the channel is given by[28]

$$\boldsymbol{u}_\infty(\boldsymbol{y})=2\sum_{i=1}^{m}\int_{L_i}\boldsymbol{q}_\infty(\boldsymbol{x})\cdot\tau^{2D}(\boldsymbol{x}-\boldsymbol{y})\cdot\boldsymbol{n}(\boldsymbol{x})ds_{\boldsymbol{x}} \tag{1}$$

where $\boldsymbol{q}_\infty$ is a yet-unknown potential density, m is the number of panels of the whole channel contour L, $\boldsymbol{n}(\boldsymbol{x})$ is the outward unit normal to the contour L (representing the different panels in Figure 1), ds_x is the length element, τ^{2D} is the fundamental stresslet in 2-D

$$\tau^{2D}(\mathbf{r})=\frac{1}{\pi}\frac{\mathbf{rrr}}{r^4} \tag{2}$$

$\mathbf{r}=\boldsymbol{x}-\boldsymbol{y}$ is the vector from the observation point to the integration point, and $L_i=L_1, L_2, \ldots$ are the line segments representing the channel boundary as shown in Figure 1 (i.e., L_1 is the line segment from vertex 1 to vertex 2, etc.). Parabolic velocity profiles for $\boldsymbol{u}_\infty(\boldsymbol{y})$ are assumed on the entrances and exit, and $\boldsymbol{u}_\infty=0$ on the walls due to the no-slip condition.

The motion of fluid within the channel requires determination of the density function, $\boldsymbol{q}_\infty(\boldsymbol{x})$, which varies over the device surface. The deflated boundary-integral equation for $\boldsymbol{q}_\infty(\boldsymbol{x})$ is obtained from Eq. 1 in a standard way.[29–31] The potential density, $\boldsymbol{q}_\infty(\boldsymbol{x})$, is first expressed in terms of a new unknown, $\tilde{\boldsymbol{q}}_\infty(\boldsymbol{x})$

$$\boldsymbol{q}_\infty(\boldsymbol{x})=\tilde{\boldsymbol{q}}_\infty(\boldsymbol{x})-\frac{1}{2}\tilde{\boldsymbol{q}}'_\infty(\boldsymbol{x}) \tag{3}$$

where $\tilde{\boldsymbol{q}}'_\infty(\boldsymbol{x})$ is the "rigid-body" projection of $\tilde{\boldsymbol{q}}_\infty(\boldsymbol{x})$. The new density $\tilde{\boldsymbol{q}}_\infty(\boldsymbol{x})$ satisfies the equation[28]

$$\tilde{\boldsymbol{q}}_\infty(\boldsymbol{y})=\boldsymbol{u}^{\mathrm{b}}(\boldsymbol{y})-2\int_L\tilde{\boldsymbol{q}}_\infty(\boldsymbol{x})\cdot\tau^{2D}(\mathbf{r})\cdot\boldsymbol{n}(\boldsymbol{x})ds_x$$
$$+\tilde{\boldsymbol{q}}'_\infty(\boldsymbol{y})-\frac{\boldsymbol{n}(\boldsymbol{y})}{L}\int_L\tilde{\boldsymbol{q}}_\infty(\boldsymbol{x})\cdot\boldsymbol{n}(\boldsymbol{x})ds_x, \tag{4}$$

where L is the contour length, and $\boldsymbol{u}^{\mathrm{b}}(\boldsymbol{y})$ are prescribed values of $\boldsymbol{u}_\infty$ on the channel boundaries. Once the density $\boldsymbol{q}_\infty(\boldsymbol{x})$ is found, Eq. 1 is used to calculate the fluid-only velocity field inside the channel. A suitable numerical method for this 2-D problem, which accounts for the presence of sharp corners between neighboring contour segments and large variations of the channel geometry, is detailed in Zinchenko et al.[28]

The 3-D boundary-integral equations are used to provide the translational and rotational velocities of a particle placed in this flow, and a moving-frame BIM as developed by Zinchenko et al.[28] is used. The fluid velocity inside the cell S_c surrounding the particle (with the cell dimensions being much larger than the particle size, but still much smaller than the overall channel size) is sought as[28]

$$\boldsymbol{u}(\boldsymbol{y})=\boldsymbol{u}_\infty(\boldsymbol{y})+2\int_{S_\infty+S_p}\boldsymbol{q}(\boldsymbol{x})\cdot\tau^{3D}(\mathbf{r})\cdot\boldsymbol{n}(\boldsymbol{x})dS_x \tag{5}$$

where $\mathbf{q}(\mathbf{x})$ is a yet-unknown potential density, $\tau^{3D}(\mathbf{r})$ is the 3-D fundamental stresslet, S_p is the particle surface, and S_∞ is the side surface of the cell, which is composed of flat panels making up the cell boundary (as explained elsewhere,[28] the contributions of the top and bottom boundaries of the cell can be neglected). The 3-D fundamental stresslet is given by

$$\tau^{3D}(\mathbf{r})=\frac{3}{4\pi}\frac{\mathbf{rrr}}{r^5} \tag{6}$$

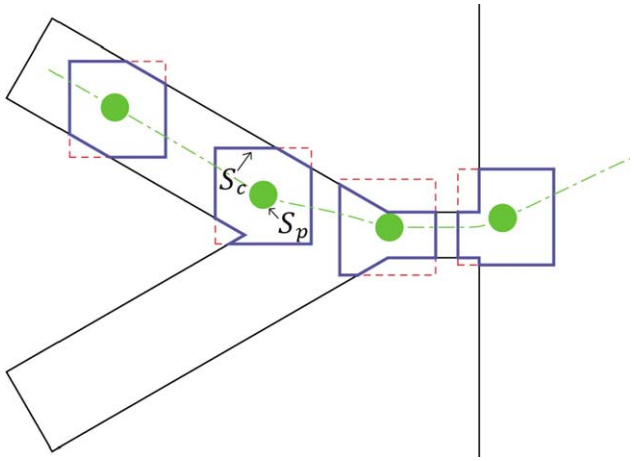

Figure 2. Schematic showing a succession of four computational cells as a particle moves through the PFF device.

The trajectory of the particle (S_p is the particle surface) is designated by the dash-dot curve, and the cell boundaries (S_c) are shown by bold lines. The dashed lines represent the portions of the square frames that are outside the PFF domain and hence, not analyzed. The frames are in fact cubes, with additional sides above and below and parallel to the plane of the illustration. [Color figure can be viewed in the online issue, which is available at wileyonlinelibrary.com.]

The well-behaved partially deflated system of boundary-integral equations for $\boldsymbol{q}(\boldsymbol{y})$ with unique solution takes the form[28]

$$\boldsymbol{q}(\boldsymbol{y})=-2\int_{S_\infty+S_p}\boldsymbol{q}(\boldsymbol{x})\cdot\tau(\mathbf{r})\cdot\boldsymbol{n}(\boldsymbol{x})dS_{\boldsymbol{x}}$$
$$-\frac{\boldsymbol{n}(\boldsymbol{y})}{S_c}\int_{S_\infty}\boldsymbol{q}(\boldsymbol{x})\cdot\boldsymbol{n}(\boldsymbol{x})dS_x\quad\text{for}\,\boldsymbol{y}\in S_\infty \tag{7}$$

and

$$\boldsymbol{q}(\boldsymbol{y})=\boldsymbol{u}_\infty(\boldsymbol{y})+2\int_{S_\infty+S_p}\boldsymbol{q}(\boldsymbol{x})\cdot\tau(\mathbf{r})\cdot\boldsymbol{n}(\boldsymbol{x})dS_{\boldsymbol{x}}-\boldsymbol{q}'(\boldsymbol{y})\quad\text{for}\,\boldsymbol{y}\in S_p \tag{8}$$

The translational and rotational particle velocities are obtained from the solution $\boldsymbol{q}(\boldsymbol{y})$ as

$$\boldsymbol{q}'(\boldsymbol{y})=\boldsymbol{V}+\Omega\times(\boldsymbol{y}-\boldsymbol{x}_c) \tag{9}$$

with $\boldsymbol{x}_c$ being the particle center.

In the moving-frame BIM, a computation cell encloses the particle at each instant of time, and the fluid velocity on the cell boundary is given by the 2-D solution for fluid-only flow. Thus, the cell boundaries that cut through the fluid must be at least several radii from the particle. Figure 2 illustrates the use of cell constructs surrounding the sphere for the moving-frame BIM. The trajectory of the particle is calculated by sequentially determining the particle velocity and location within each cell.

Numerical considerations

The numerical solution of the boundary-integral equations requires discretization of the channel and particle surfaces. A meshing bias is used to increase computational efficiency,

Table 1. Typical Meshing for the PFF Device by Region

Channel Region	Panel	Panel Length	Number of Increments
Pinch	6, 12	$2H_p$	500
Inlet	1	$2H_p$	500
	2	$6H_p$	1500
	13	$8.46H_p$	2115
Sweep	4	$2H_p$	500
	3	$6H_p$	1500
	5	$8.46H_p$	2115
Exit	7	$9.5H_p$	1781
	8	$30H_p$	5625
	9	$20H_p$	3750
	10	$30H_p$	5625
	11	$9.5H_p$	1781

The panels correspond to the first vertex number of each panel, moving counter-clockwise around the channel, beginning with vertex 1 (shown in Figure 1). The increment length is the panel length divided by the number of increments.

with the panels for the inlet channels and pinch area having a greater number of meshing units per length of contour than those in the exit portion of the device. For the 2-D solution for fluid only, the inlet, pinch, and exit panels of the overall channel are divided into increments with lengths made dimensionless by the pinch height, H_p. A greater emphasis is given to the inlet and pinch segments, as shown in Table 1 for a typical case.

Six different geometries of the PFF device were considered in the simulations:

1. Base geometry: For the base case, which corresponds to the dimensions in Table 1, $H_i = 2H_p$, $L_i = 8.46H_p$, $\theta_i = 60°$, $L_p = 2H_p$, $H_e = 20H_p$, $L_e = 40H_p$, and $\theta_e = 90°$.
2. Angled exit: For this case, the geometry is the same as the base case, except $\theta_e = 45°$.
3. Elongated pinch: For this case, the geometry is the same as the base case, except $L_p = 4\ H_p$.
4. Narrow inlet: For this case, the geometry is the same as the base case, except $H_i = H_p$.
5. Wing geometry: For this case, the geometry is the same as base case, except $\theta_e = 135°$.
6. Beveled exit corner: For this case, the geometry is the same as base case, except the sharp corner at the exit of the pinch is replaced with a 45° beveled edge.

To simulate particle trajectories, a 3-D particle is placed in the 2-D, fluid-only environment. For the cell wall, the mesh was generated using the gap-adaptive surface discretization as described by Zinchenko et al.[28] The surface of the particle is meshed using N_Δ triangles. Meshing of the particle surfaces for the BIM is based on providing acceptable numerical accuracy for simulations within computational limits. We found that $N_\Delta = 3840$ was sufficient to give results that converged to within 0.05%. All of the calculations for this work used uniform meshing for the spheres, although a future improvement might be to use an adaptive mesh with greater refinement in areas where the sphere is close to the wall. All numerical calculations were generated using single-core (logical) calculations with an Intel Core 975 CPU (4.2 GHz) using PGI accelerator Visual Fortran, release 11.5.

Experimental Methods and Materials

Microchannel device fabrication

A photopolymerizable, thiol-ene based resin was used to fabricate the PFF device. An aromatic urethane diacrylate (Ebecryl 4827) was donated by Cytec Surface Specialties (Smyrna, GA), and pentaerythritol tetra(3-mercaptoproprionate (PETMP) was donated by Evans Chemetics (Waterloo, NY). Triallyl- 1,3,5- triazine 2,4,6 trione (TATATO) was purchased from Sigma-Aldrich (Milwaukee, WI). The inhibitor, *N*-nitrosophenyl-hydroxylamine (Q1301), was donated by Wako Pure Chemicals (Osaka, Japan) and the photoinitiator, Irgacure 651, was donated by Ciba Specialty Chemicals (Tarrytown, NY). All materials were used as received without additional purification.

The previously developed, soft-lithography fabrication method known as contact liquid photolithographic polymerization (CLiPP)[32,33] was used to produce the device where a modified, one-step "sandwich" method (Figure 3) was used to fabricate channels with narrow channel features ($<10^{-4}$ m width). Glass cover slides were cleaned by etching with a solution consisting of one part hydrogen peroxide and three parts sulfuric acid for 3 h. The slides were then washed with deionized water and acetone. After cleaning, the slides were coated with methacryloxypropyl-trimethoxysilane (MPS) (Gelest, Morrisville, Pa.) by surface-layer deposition, which involved placing the cleaned cover slides with 3 mL of MPS inside a sealed Teflon container. The Teflon container was placed inside an oven and heated to 70°C for 4 h. Subsequently, the monomer formulation was injected between the two treated glass cover slides, with a photolithographic mask attached to the surface. Masks were created with feature resolution of 3×10^{-5} m (printed masks), and the masks were used to fabricate the PFF channel geometries. The monomer mixture was exposed to a collimated light source in a mask alignment system (Optical Associates, San Jose, CA) using a collimated flood exposure source with area of 5×10^{-2} m by 5×10^{-2} m and irradiation intensity of 3.75 W/m^2 having a principal output at 365 nm. Irradiation intensities were measured using an International Light, model IL1400A radiometer (Newburyport, MA). Following the cure process, any uncured monomer mixture was removed by flushing the nascent device with methanol followed by removal of excess solvents and monomer, leaving only the desired photopatterned, crosslinked polymer device.

Cure time for the device was determined using a method developed to optimize feature fidelity.[34] For a device having a pinch height of 1×10^{-3} m and width of 4×10^{-3} m, an optimal cure time of 37 s was used with a 3.75 W/m^2 light source.

A single pinched-flow geometry was constructed, with channel dimensions of $H_p = 1 \times 10^{-3}$ m, $L_p = 2H_p$, $H_i = 2H_p$, $L_i = 8.46H_p$, $H_e = 20H_p$, $L_e = 40H_p$, $\theta_i = 60°$, and $\theta_e = 90°$. The width or depth of the channels in the direction perpendicular to the plane shown in Figure 1 is $W = 4 \times 10^{-3}$ m. This size is larger than those used for typical microfluidic devices, to provide ease of visualization and to reduce the effects of surface roughness. Appropriately larger size particles were used to preserve the desired pinch height to particle size ratio.

Particle tracking

Polystyrene particles (Polysciences, Warrington, PA) with diameters in the range 2×10^{-4} m $2a \leq 5 \times 10^{-4}$ m were analyzed and separated in the PFF device. The particle density is 1.05×10^3 kg/m^3, and the particles were suspended in a fluid consisting of 22 weight percent glycerol in water, with a fluid density matching that of the particles. The

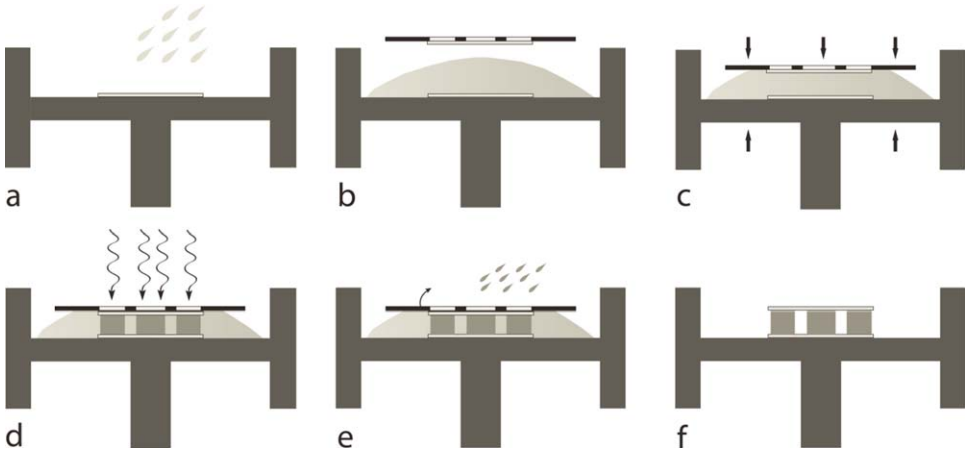

Figure 3. Schematic of the CLiPP process.

Step a: The siloxane-treated glass slide is secured to the chamber base and a monomer mixture fills the chamber. Step b: After filling the chamber with monomer, an aligned mask (top) is joined with a siloxane-treated glass slide and placed over the monomer. Step c: The siloxane-treated glass slide is brought in contact with the monomer mixture and lowered to the desired feature height. Step d: The monomer mixture is exposed to 365 nm UV radiation through the aligned mask. Step e: The mask is removed from the glass slide. Step f: Excess, uncured monomer mixture is removed by washing with solvent. After washing, only the substrate, top glass slide and PFF device remain. [Color figure can be viewed in the online issue, which is available at wileyonlinelibrary.com.]

viscosity of the mixture was 1.7×10^{-3} kg/(m s) at the ambient temperature of 23 ± 1°C. Two polystyrene bead sizes ($\eta = 2a/H_p = 0.25$ and 0.5, respectively) were suspended in the inlet solution. Dilute concentrations of 10 spheres per mL of solution were created by mixing the polystyrene beads with the water/glycerol solution for 20 min, so that individual spheres could be tracked without particle–particle interactions, as simulated by the model. Volumetric flow rates for the sweep stream were varied from 5 to 15 mL/min, with flow ratios ranging from 2 to 35.

Tracking of the particles during transport was accomplished using an experimental setup as shown in Figure 4. A pump controller [Bee Hive; Bioanalytical Systems (BAS)] was used to control the volumetric flow rates from two disposable 5-mL syringes (Becton-Dickinson, Franklin Lakes, NJ). Each syringe was placed onto a syringe drive (Baby Bee; BAS, West Lafayette, IN), connected to the pump controller by an RJ-45 cable. The Bee pump control system provided independent control of the fluid-only sweep stream (Q_s), and the fluid/particle mixture inlet stream (Q_i) flow rates. Flow rates were set using a variable knob-adjustment controlling the rate of fluid injection of each 5-mL syringe. Tygon tubing with 3/32″ OD was joined to the syringe using a Luer-lock connection. The Tygon tubing was connected to an 18-gauge needle using an additional Luer-lock connection. Calibration of the syringe pumps was carried out by measuring the volumes of fluid collected for time periods of 5, 10, and 20 min, which showed consistent delivery over time.

The PFF device was mounted onto the stage of a Nikon TE300 microscope (Nikon TE300, Melville, NY). The

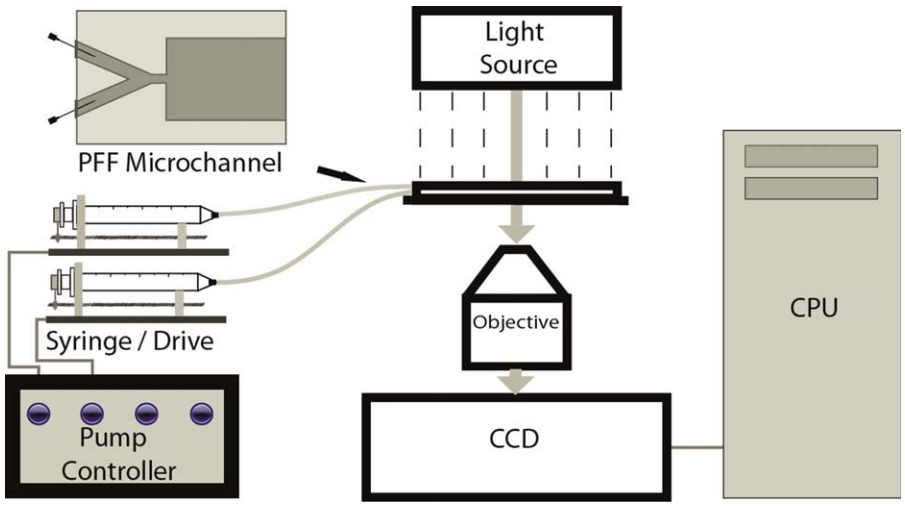

Figure 4. Schematic of experimental setup used to track particle trajectories.

A top view of the PFF device is shown in the upper left corner. Two syringes provide fluid and fluid/particle suspension injected into separate inlet channels of the PFF device. Syringe injection is controlled by a pump controller (lower left-hand corner). The PFF microchannel is fixed to a microscope stage below a light source and above the microscope objective (middle of figure). Images of particle movement are captured by a video camera and transmitted to a PC (right side). [Color figure can be viewed in the online issue, which is available at wileyonlinelibrary.com.]

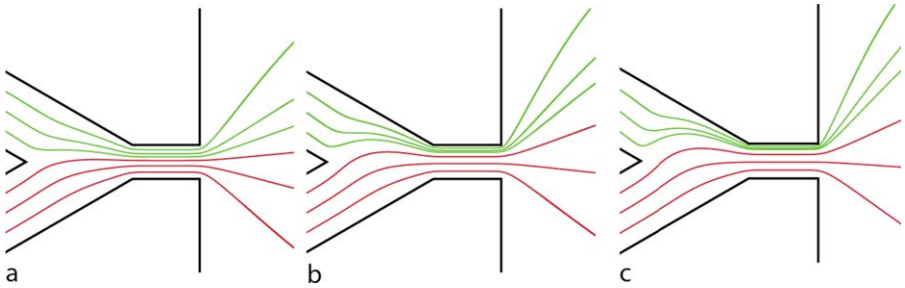

Figure 5. Inlet and pinch areas of a PFF device showing fluid-only streamlines for $Q_s/Q_i = 2.0$, 6.0, and 10.0 (left to right).

The device geometry uses the base case, where $H_i = 2H_p$. [Color figure can be viewed in the online issue, which is available at wileyonlinelibrary.com.]

microscope objective (4X, Nikon Achromat, NA 0.10, WD 30) faced upward, toward the PFF. Digital imaging and data collection were carried out using a video camera (KP-M2, Hitachi Corporation, Chula Vista, CA) with 2X intermediate magnification. Data analysis was accomplished using Metamorph imaging software (Universal Imaging Systems, Downington, PA).

Simulation Results and Discussion

Example fluid streamlines

2-D examples of the simulation for fluid-only streamlines in the PFF using BIM are provided in Figure 5, which shows the pinch and adjacent areas of the PFF device, for flow ratios of $Q_s/Q_i = 2.0$, 6.0, and 10.0. At a flow ratio of 2.0, as shown in Figure 5a, the streamlines originating from the upper, inlet stream are compressed less in the pinch area than those with higher flow ratios. Thus, it is expected that higher flow ratios will give better particle separation due to steric hindrance as particles of different sizes are pressed against the top wall of the pinch region. On the other hand, high flow ratios may be undesirable due to dilution of the particle stream, and so optimal conditions to obtain the desired separation at the lowest possible flow ratios are sought.

Example particle trajectories

Figure 6 shows example particle trajectories from the BIM simulations that demonstrate the separation of particles by size. In this example, all particles start at the centerplane of the inlet channel. As expected, the smaller spheres move toward the upper portion of the exit area, while the larger particles move closer to the center of the exit area. Note that the smallest particles closely follow the fluid streamline, whereas the departure of the particle trajectories from the fluid streamline increases with particle size due to steric exclusion.

Figure 7 further illustrates particle separation by size. It shows the lateral exit positions of particles of different sizes that started at the inlet centerplane. As noted previously, the smallest particles exit on the highest trajectory because their centers are able to approach most closely to the upper wall of the pinch. As the flow ratio is increased, the smaller particles are pressed closer to the upper wall, and so exit at an even higher position, whereas the largest particles are already as close as allowed to the upper wall and so exit at the same position. Thus, separation improves with increasing flow ratio, until all particles are pressed as close as possible to the upper wall.

Particle trajectory "banding" and critical flow ratio

The trajectories shown in the previous section are for particles starting on the inlet channel centerplane. However, in practice the particles will enter across the entire entrance, with their centers ranging from one radius above the lower wall to one radius below the upper wall (plus any small surface roughness or other exclusion effect imposing a minimum surface clearance). Hence, a "band" of trajectories is observed for each particle size. Such bands are shown in Figure 8 for two particle sizes. In general, the band is lower for the larger particles due to steric hindrance by the upper wall of the pinch. For the relatively low flow ratio of $Q_s/Q_i = 3.385$ in Figure 8 (left), the bands overlap in the exit region, illustrating incomplete separation. However, at the higher flow ratio of $Q_s/Q_i = 6.0$ in Figure 8 (right), the bands do not overlap and complete separation is predicted. Moreover, the larger particles shown in Figure 8 (right) all

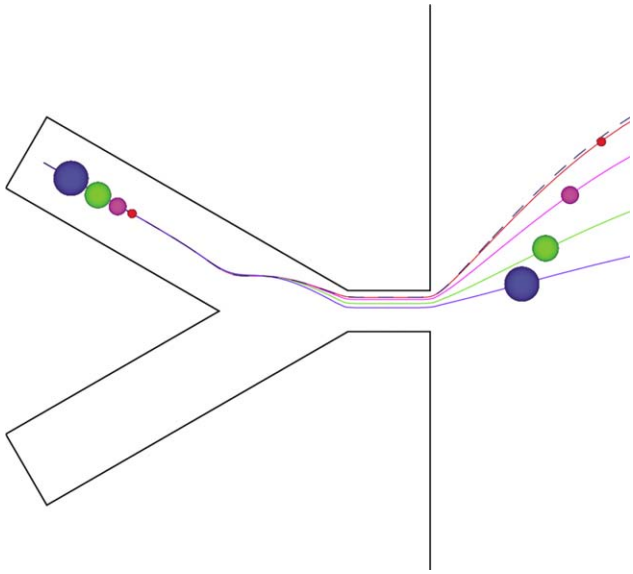

Figure 6. Trajectory paths for spheres entering along centerplane of the inlet channel, with flow ratio $Q_s/Q_i = 6.0$.

Sphere sizes of $\eta = 0.2$, 0.4, 0.6 and 0.8 are included, and the fluid-only streamline (dashed line) is also shown. The device geometry uses the base case. [Color figure can be viewed in the online issue, which is available at wileyonlinelibrary.com.]

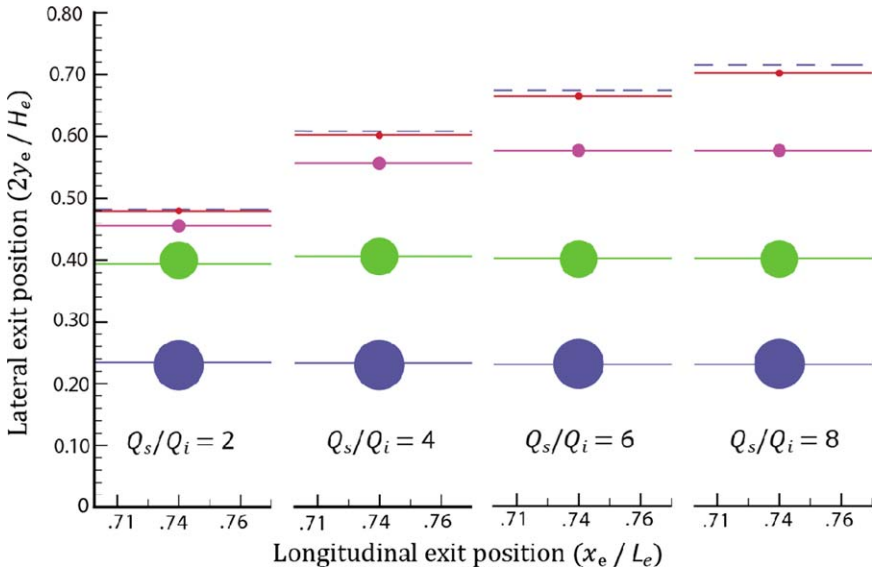

Figure 7. Lateral exit position distribution of particles starting at the inlet centerplane and with $\eta = 0.2$, 0.4, 0.6, and 0.8 (top to bottom) for $Q_s/Q_i = 2.0$ (left), 4.0 (second), 6.0 (third), and 8.0 (right).

The base geometry is used and all particles enter the inlet with particle centers located on the midplane. Lateral and longitudinal positions are normalized with respect to pinch height H_p. The dashed line shows the fluid-only streamline with the same starting position as the particles. Here, y_e is the vertical distance above the channel midplane, and x_e is the horizontal distance from the pinch exit. [Color figure can be viewed in the online issue, which is available at wileyonlinelibrary.com.]

proceed through the exit on a single trajectory, because the sweep flow is sufficiently strong to press all of the larger particles to the upper wall of the pinch region—independent of their entrance position.

Figure 9 shows the lateral exit position vs. inlet position. Here, $P_i = (y_i - a)/(H_i - 2a)$, where y_i is the initial distance of the particle center above the lower inlet wall. As noted previously, the smaller particles have higher exit locations, and the lateral exit location increases with increasing entrance location above the lower wall. Of particular interest is that a plateau is observed for each particle size, where the exit position becomes independent of the entrance position. The plateau occurs because all particles entering above a critical location come in contact with the upper wall of the pinch. The critical entrance location is determined by using "backward" integration of the trajectory from particle contact with the corner (vertex 12 in Figure 1). The larger particles come in contact with the upper wall of the pinch at lower inlet positions due to greater steric exclusion. Similarly, the exit plateau occurs at lower inlet positions when the flow ratio is increased, as the particles are then more strongly pressed against the upper wall of the pinch region by the sweep fluid. At a high enough flow ratio and/or particle size, all particles of a given size reach the upper wall and exit on a single trajectory rather than within a band of trajectories, as shown for the larger particles in Figure 9.

An average lateral exit position at a fixed distance downstream from the pinch exit may be determined:

$$\langle y_e \rangle = \int_0^1 y_e(P_i) dP_i \tag{10}$$

where it is assumed that all physically possible entry positions are equally probable. This average exit position is

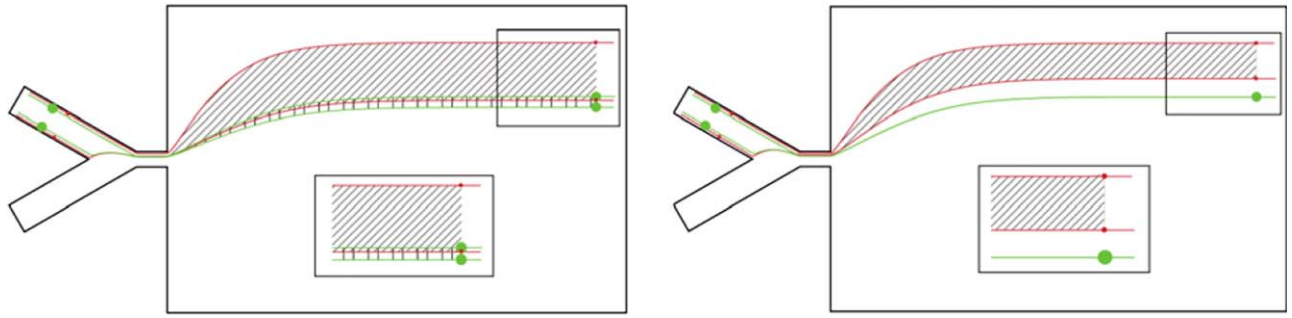

Figure 8. Banding effect illustrated, where spheres of two sizes, $\eta = 0.2$ and 0.6, enter near the top and bottom of the inlet channel at flow ratio = 3.385 (left) and 6.0 (right).

Solid curves (red and green for $\eta = 0.2$ and 0.6, respectively, on the color version) indicate trajectories of the spheres. At lower flow ratios, incomplete separation takes place, resulting in a "band" of mixed spheres in the area marked by a mix of diagonal and vertical lines (as shown by inset on left), while at higher flow ratios, complete separation of particles takes place (as shown by inset on right). In each case, the inset shows an expanded view of the trajectory "bands" exhibited by the spheres at a given flow ratio. For this illustration, the base-case geometry is used. [Color figure can be viewed in the online issue, which is available at wileyonlinelibrary.com..]

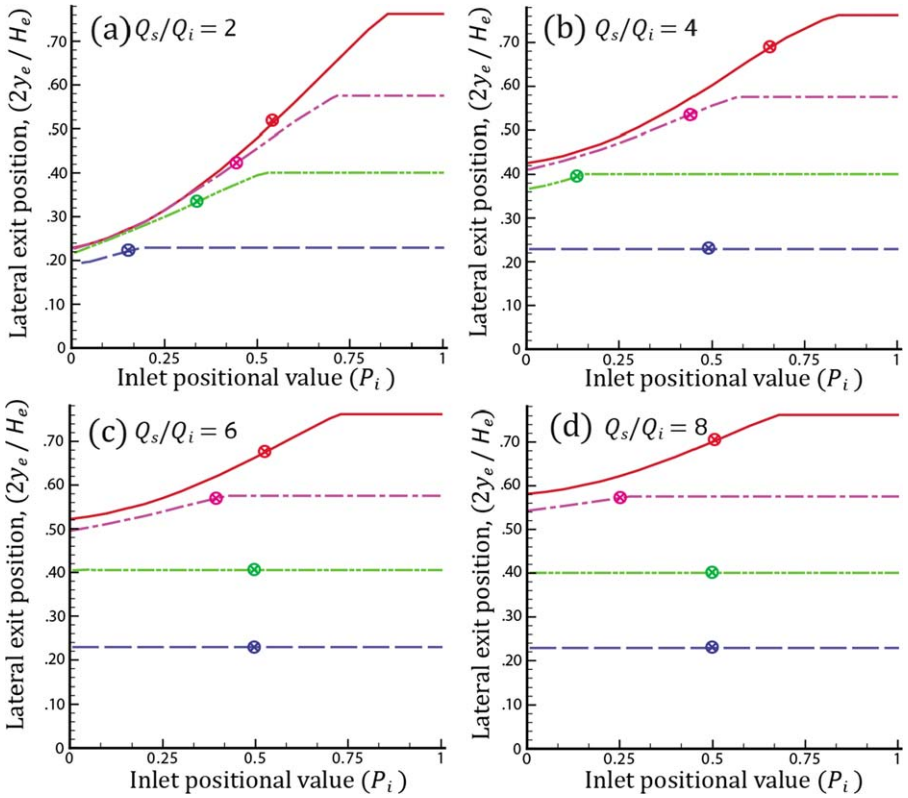

Figure 9. Exit position vs. entrance position for particles of size $\eta = 2a/H_p = 0.2$, 0.4, 0.6 and 0.8 (top to bottom) and flow ratios of Q_s/Q_i = (a) 2, (b) 4, (c) 6, and (d) 8.

The average exit position, $\langle y_e \rangle$, is denoted by $\otimes$. The device geometry uses the base case. [Color figure can be viewed in the online issue, which is available at wileyonlinelibrary.com..]

also shown in Figure 9, and it increases with decreasing particle size.

As evident from Figure 9, particles of a given size reach the upper wall of the pinch at sufficiently high inlet positions and flow ratios, and then depart at the same downstream trajectory from vertex 12. For a given particle size, there is a critical flow ratio, $(Q_s/Q_i)_c$, above which all particles reach the upper wall and depart on the same downstream trajectory, even if the particles enter near the bottom of the inlet channel. In Figure 10, this critical flow ratio is plotted vs. particle size. The critical flow ratio decreases with increasing particle size, as the larger particles more easily reach the upper wall. These results have important practical value, because operation at the critical flow ratio, rather than a higher or lower value, for a given particle size ratio allows for those particles to be collected in a narrow exit drain with minimal dilution by the sweep fluid.

Corner effects

Figure 11 illustrates the critical trajectory of a sphere with $\eta = 0.6$ as it comes in contact with the walls and corners of the pinch region. A minimum sphere-wall gap of $0.01a$ is used in this example, such as might be the case if there are surface roughness elements with heights of 1% of the particle radius, and it is assumed that the sphere comes into contact with the wall when this minimum gap is reached. Once the sphere comes in contact with a wall, it moves parallel to the wall until reaching a corner. The sphere then pivots about the corner until hydrodynamic forces pull it away from the corner. The "departure" angle (relative to the normal from the wall) is where the sphere departs from the corner and is described by $\theta_{v,dep}$, with v denoting the vertex number.

Table 2 illustrates the relationship between the critical angle and particle size of spheres exiting the pinch. As particle size increases, so does the associated departure angle at the pinch exit, as the fluid streamlines and particle

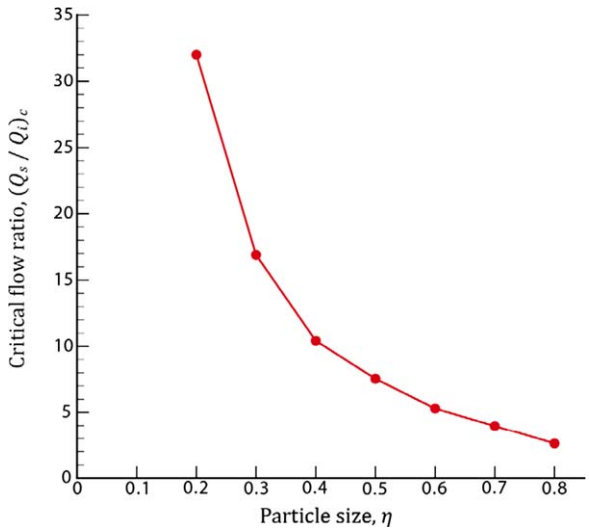

Figure 10. Critical flow ratio $(Q_s/Q_i)_c$ for a single exit trajectory vs. dimensionless particle size $\eta = 2a/H_p$.

[Color figure can be viewed in the online issue, which is available at wileyonlinelibrary.com.]

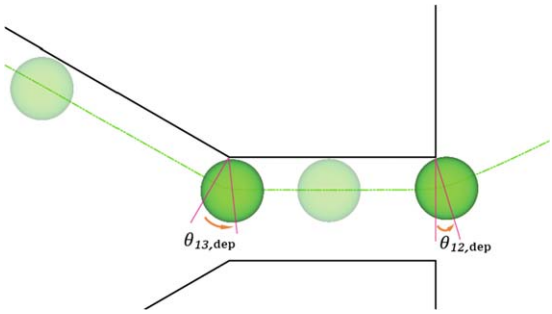

Figure 11. A $\eta = 0.6$ sphere at $Q_s/Q_i = 3.86$ coming into close contact with the upper walls and then pivoting about the entrance and exit corners of the pinch region.

The departure angle, $\theta_{v,dep}$, at which the sphere moves away from the corner, is illustrated. The trajectory path is shown by the curve. [Color figure can be viewed in the online issue, which is available at wileyonlinelibrary.com.]

trajectories have less curvature further from the corner (see Figures 5 and 6). Values for $\theta_{12,dep}$ change very little with an increase or decrease in flow ratio, as the fluid flow is fully developed (i.e., independent of inlet conditions) by the pinch exit.

Figure 12 shows the trajectories of the spheres after they leave the corner at the pinch exit. For smaller spheres, the fluid-only streamline approximates the sphere trajectory. As the sphere radius increases, the trajectory deviates more from the fluid-only streamline. The fluid streamlines and particle trajectories are essentially independent of the flow ratio, because the flow is fully developed by the exit of the pinch and so independent of inlet conditions. Fluid-only streamlines are farther from the upper exit wall than the associated particle trajectory. Lubrication effects associated with particle–wall interactions result in a lag in release of the particle as they exit the pinch area, and the particle–wall interactions increase with particle size.

Particle separation

As was seen in Figure 9, complete separation of two particle sizes may be achieved at sufficiently high flow ratios. We define the separation flow ratio, $(Q_s/Q_i)_s$, such that complete particle separation by size occurs above this value. Figure 13 illustrates conditions (a) below the separation flow ratio, (b) at the separation flow ratio $Q_s/Q_i = 3.87$, and (c) above the separation flow ratio. At a flow ratio less than the separation flow ratio, mixing of the particle bands occurs, while at a flow ratio above the separation flow ratio, complete separation occurs. The concept of "banding" of exit trajectories based on the distribution of particles of a given size and entry position across the inlet channel provides the basis for determining the minimum flow ratio needed for complete separation of particles, $(Q_s/Q_i)_s$. As shown in Figure 13, we consider a larger particle that enters the inlet channel at $P_i = 0.99$ near the upper wall, representing the top of the band of larger particles. The smaller particle enters the inlet channel at $P_i = 0.01$ near the lower wall, representing the lower trajectory of the smaller particle band. Here, it is assumed that there is surface roughness or repulsion that prevents particles from being less than 1% of its radius from the wall. In Figure 13a, the smaller particle is below the larger particle in the exit, whereas it is above the larger particle in Figure 13c. In Figure 13b, where $Q_s/Q_i = (Q_s/Q_i)_s$, the lowest small particle and the highest large particle achieve the same exit position. The separation flow ratio was determined by the Newton–Rhapson iteration of the numerical results.

Figure 14 gives the separation flow ratios for pairs of dimensionless particle sizes ranging from $\eta = 0.2$ to $\eta = 0.8$. The value of $(Q_s/Q_i)_s$ decreases with increasing size of the larger particle, because the exit trajectory is lowered due to steric exclusion when the size of the larger particle is increased, making it easier for smaller particles to cross the trajectory with a lower flow ratio. This result indicates that the pinch region should have a height that is only slightly larger than that of the largest particles, to minimize the amount of sweep fluid used during operation. In contrast, $(Q_s/Q_i)_s$ increases weakly with an increase in the size of the smaller particle. The weak dependence on size of the smaller particle is due to the fact that its separation trajectory does not reach the pinch wall; hence, it does not have steric exclusion. However, there are hydrodynamic interactions between the particles and upper wall, which increase with the particle size and thereby require a slightly higher flow ratio to push all of the small particles above the highest large particle. An important finding from Figure 14 is that the separation flow ratio needed to achieve complete separation is less than the critical flow ratio (for all particles to reach the upper wall and depart on a single trajectory for each particle size—see Figure 10). This finding implies that less sweep fluid is required for complete separation than for the bands to collapse to single exit trajectories, but the exit drains must be larger to collect the particles from these bands than from single exit trajectories.

Channel geometry effects

To study the effects of channel geometry on particle trajectories and separation, changes were made to the inlet, pinch, and outlet areas of the PFF geometry. Figure 15 shows the results from the simulations to determine the required separation flow rates from the different geometric configurations considered. Lengthening the pinch region or making the inlet channels more narrow (not shown) has only a small effect, which is not unexpected, given the results in Figures 5 and 6 showing that the fluid streamlines and particle trajectories become parallel to the channel walls almost immediately upon entering the pinch, so that the flow is fully developed at the pinch exit and independent of initial conditions. In contrast, an angled exit with $\theta_e = 45°$ gives poorer separation than does the base case with $\theta_e = 90°$, requiring larger flow ratios to achieve complete separation. The reduced performance is because the angled exit does not provide as much separation of the trajectories of particles of different sizes as they pivot around the corner (vertex 12) and leave the pinch region for the exit region. In particular, the angled wall is closer to the particles and causes resistance as they pull away from the corner, so that the particle trajectories are higher than the streamlines, as shown in Figure 16. This effect is greatest for the larger particles, reducing their

Table 2. Variation of the Departure Angle with Particle Size at the Pinch Exit

η	0.2	0.3	0.4	0.5	0.6	0.7	0.8
$\theta_{12,dep}$	14.0°	18.0°	19.2°	22.5°	23.6°	24.6°	28.1°

Figure 12. Comparison of particle trajectories (solid curves) to fluid-only streamlines (dashed curves) for particle sizes $\eta = 0.2$, 0.4, 0.6, and 0.8 (top to bottom), with $Q_s/Q_i = 2.0$ (left) and 10.0 (right).

The fluid streamlines and particle trajectories originate at the exit of the pinch at a distance of 1.01*a* directly below the upper-corner of the pinch exit. The base geometry configuration is used for this illustration. [Color figure can be viewed in the online issue, which is available at wileyonlinelibrary.com.]

separation from the smaller particles. Finally, the wing exit with $\theta_e = 135°$ has almost the same separation (Figure 15) as the base case, because the angled wall in this case has almost the same small effect on the particle trajectories (Figure 16) as does the vertical wall with $\theta_e = 90°$.

To ascertain the cause of lower separation efficiency exhibited by the angled exit, we examined whether a small change in the corner geometry would have a similar impact as modifying the full length of the wall adjacent to the pinch exit. For Figure 16d, the 90° sharp corner was replaced with a 45° beveled edge having a length equal to 0.75*a* for a particle with $\eta = 0.6$. The deviation of the particle trajectory from the fluid streamline is slightly less than that shown by the angled exit configuration, but much greater than that shown with the base case geometry. Lubrication effects are stronger between the particle and the beveled edge than between the particle and sharp corner, thereby causing the greater deviation of the particle trajectory from the fluid streamline. The simulation illustrates the pronounced effect that an irregularity at the pinch exit may have on the particle trajectory and device performance. As the length of the beveled edge is reduced, so are the particle–wall interactions, resulting in an increase in separation efficiency (not shown).

Particle selectivity and recovery

For some applications, complete separation of particles by size is not necessary or may not be desired. A predetermined ratio of small particles relative to larger particles may be achieved by varying the flow ratio. Moreover, the resulting mixture of particles exiting the PFF in a narrow trajectory band is more concentrated than the mixture entering the device. In this section, we show how the particle recovery and mix ratio may be determined when there is incomplete separation.

For simplicity, we consider two particle sizes and two product or exit streams, although the principles below may be easily extended to multiple particle sizes and/or product streams. Let y_e* be the location of the "splitter" in the exit area that separates the top and bottom product streams. To calculate the recovery of the particles of a given size in each product stream, we need to find the entry position (designated as y_i*) that corresponds to a lateral exit position of y_e*, as illustrated in Figure 17. This determination may be found by backward integration of the particle trajectory from the exit to the inlet.

The recovery of particles of the given size i in the top product stream is then simply the fraction of particles of size i that enter the inlet channel at locations above y_i^*

$$R_i^{Top} = \frac{\int_{y_i^*}^{H_i - a_i} C_i(y_i) V_i(y_i) dy_i}{\int_{a_i}^{H_i - a_i} C_i(y_i) V_i(y_i) dy_i}, \tag{11}$$

where H_i is the inlet height and y_i is the distance from the lower wall of the inlet to the center of a particle of radius a_i, with C_i and V_i being the concentration and longitudinal velocity, respectively, of particles of radius a_i in the inlet. If we further assume that the entry flux is uniform so that the product $C_i(y_i)Vi(y_i)$ is constant for $a_i < y_i < (H_i - a_i)$, then Eq. 11 reduces to

$$R_i^{Top} = (H_i - a_i - y_i)/(H_i - 2a_i). \tag{12}$$

Of course, the recovery of particles of size i in the bottom product stream is simply

$$R_i^{Bot} = 1 - R_i^{Top}. \tag{13}$$

Then, the fraction of particles of size i in the bottom product stream, by either number or mass, is

$$F_i^{Bot} = F_i^{Feed} R_i^{Bot} / R_j^{Bot}, \tag{14}$$

where F_i^{Feed} is the fraction of particles of size i (by number or mass) in the inlet feed stream, and R_j^{Bot} is the recovery of particles of size j in the bottom product stream.

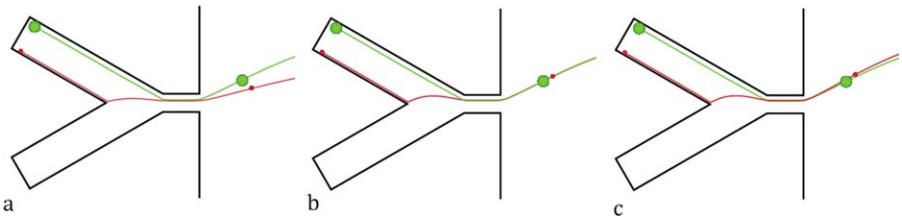

Figure 13. Effect of increased flow ratio on $\eta = 0.2$ and $\eta = 0.6$ (red and green, respectively, on the color version) particle trajectories, with (a) $Q_s/Q_i = 3.64$, (b) $Q_s/Q = (Q_s/Q_{ij} = 3.87$, and (c) $Q_s/Q_i = 4.06$.

The separation flow ratio is $(Q_s/Q_i)_s = 3.87$. [Color figure can be viewed in the online issue, which is available at wileyonlinelibrary.com.]

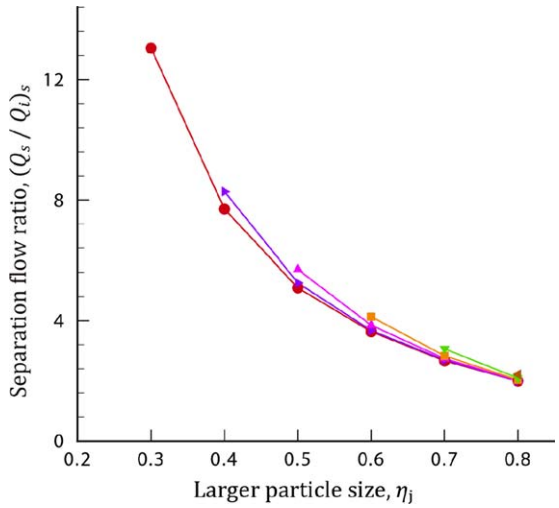

Figure 14. Separation flow ratio $(Q_s/Q_i)_s$ required for complete separation of smaller particles (η_i) from larger particles (η_j).

The dimensionless sizes of the smaller particles are $\eta_i = 0.2$ (•), 0.3 (▶), 0.4 (▲), 0.5 (■), 0.6 (▼), and 0.7 (◀).The base geometry was used. [Color figure can be viewed in the online issue, which is available at wileyonlinelibrary.com.]

Figure 18 shows numerical results for the recovery of the smaller particles in the top product stream as a function of the flow ratio of the sweep and inlet streams for several pairs of small and large particle sizes. Here, we consider the special case where the exit splitter location y_e* is placed just at the top of the band of the larger particles, so that all of the large particles are recovered in the bottom stream ($R_j^{Bot} = 1$, $R_j^{Top} = 0$). At low flow ratios, a relatively small fraction of the small particles is recovered in the top product stream, and so the bottom stream contains a mix of small and large particles given by Eqs. 12 and 13. However, the separation efficiency increases with increasing flow rate, and complete separation ($R_i^{Top} = 1$, $R_i^{Bot} = 0$) is achieved when $Q_s/Q_i \geq (Q_s/Q_i)_s$.

Experimental Results

Pump calibration/measurement uncertainty

Accurate measurement of fluid volumetric flow ratio is critical for obtaining accurate and reproducible results and the pump selection was made to assure a constant flow rate. Settings for the pump flow rate are based on the syringe volume. The pumps were calibrated over 2, 10, and 20 min intervals using flow rate settings of 10, 20, and 30 μL/min for five of the experiments. Linear regression of the calibration data gives $Q_{meas} = (0.95 \pm 0.02)\ Q_{set}$ at the 95% confidence level, where Q_{set} is the manufacturer setting and Q_{meas} is the measured value of the flow rate.

Lateral exit positions of particles

Experiments using two sets of particle sizes ($\eta = 0.25$, 0.5) at subcritical and supercritical flow ratios were conducted. Lateral exit positions of the particles were compared to BIM simulations. Critical flow ratios of $(Q_s/Q_i)_c = 32.5$ and 7.73, respectively, are predicted for $\eta = 0.25$ and 0.5. Particles with $\eta = 0.25$ were tested at flow ratios of $Q_s/Q_i = 2.0$ (subcritical), 8.0 (subcritical), and 35 (supercritical), while particles with $\eta = 0.5$ were tested using flow ratios of $Q_s/Q_i = 4.0$ (subcritical), 9.0 (supercritical), and 35 (supercritical).

The lateral exit positions of the particles from the experiments and BIM simulations are compared in Table 3. Variations in particle radius are provided by the manufacturer as ≤0.1%, while variations in the channel height and particle location are ≤0.5% and attributed to pixel sizes of the mask and digital images. This table shows that the exit position increases with inlet position for subcritical flow ratios but reaches a plateau for inlet positions above a critical value where the particles reach the upper wall of the pinch. It also shows that the exit position increases with flow ratio until the critical flow ratio is reached. Most important, both theory and experiment show that the smaller particles exit on higher trajectories, so that separation is feasible. The exit locations from theory and experiment are within a few percent of each other, which may be somewhat fortuitous, as described below.

Although experimental results for lateral exit positions closely agree with the BIM simulations as shown in Table 3, the simulated and experimental particle trajectories differ. As shown in Figure 19, the smaller particles exit the device closer to the top of the exit area, while the larger particles exit further away from the top of the device, as expected. However, the simulated particle trajectories (see Figure 16a) have a more pronounced arch upon exiting the pinch, while the experimental trajectories are shallower. The experimentally observed lateral positions of the particles continue to rise as the particles traverse the exit, and ultimately reach or even cross the simulated trajectories. We believe that the

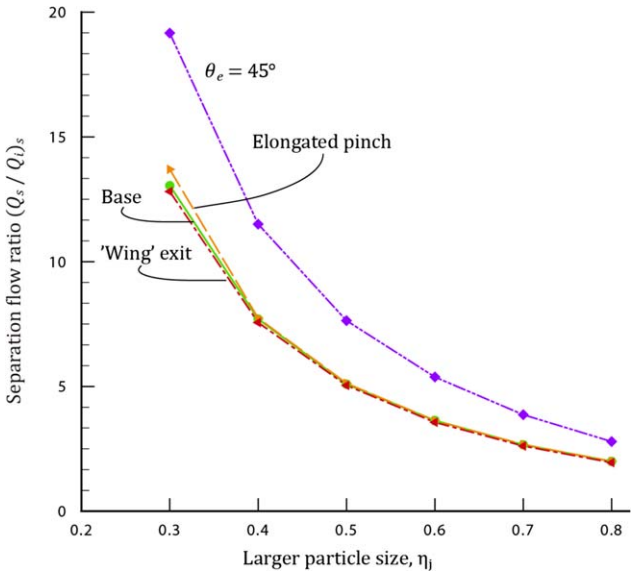

Figure 15. Separation flow ratio $(Q_s/Q_i)_s$ required to completely separate smaller particles ($\eta_i = 0.2$) from larger particles (η_j = varied) for four geometric configurations of the PFF.

The base geometry is represented by (•) with solid lines, angled exit by (◆) and dash-dot-dot lines, elongated pinch by (▶) and long-dash lines, and wing geometry by (◀) and short-dash lines. [Color figure can be viewed in the online issue, which is available at wileyonlinelibrary.com]

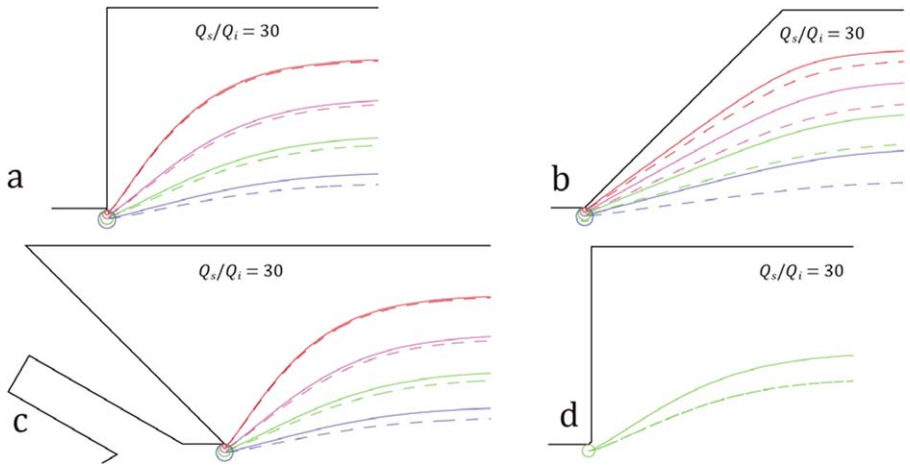

Figure 16. Comparison of particle trajectories (solid lines) to fluid-only streamlines (dashed curves) corresponding to starting positions of particle sizes $\eta = 0.2$, 0.4, 0.6, and 0.8 (top to bottom) with $Q_s/Q_i = 30$ for (a) base case, (b) angled exit, (c) winged exit, and (d) beveled corner for $\eta = 0.6$.

The fluid streamlines and particle trajectories originate at the exit of the pinch at a distance of $1.01a$ directly below the upper corner of the pinch exit. [Color figure can be viewed in the online issue, which is available at wileyonlinelibrary.com.]

differences between the simulated and experimental trajectories are due to inertial effects and the low aspect ratio of the device exit area. The simulations assumed small Reynolds number, so that inertia could be neglected. In contrast, for the experiments in Figure 19, the Reynolds number in the pinch is Re = 5.3, where $\mathrm{Re} = \rho U H_p/\mu$ and $U = (Q_s + Q_i)/(WH_p)$ is the average velocity. The inertia in the experiments causes fluid and particles to exit the pinch with flatter paths than predicted by the simulations. For the moving-frame simulations, we also assumed a high ratio of width (in the direction normal to the paper) to height. For the experiments, this aspect ratio is 2.0 in the inlet, and 4.0 in the pinch, but only 0.2 in the exit area. Thus, the assumption of a high aspect ratio and its impact on the particle trajectories is not met in the exit region, and the flow profiles (and, hence, particle trajectories) are different from the simulations. After the flow becomes fully developed in the exit, it is nearly a plug flow instead of parabolic flow in the x–y plane, with nearly parabolic flow instead in the x–z plane (where the z direction is normal to the plane of Figure 1). As a result, the fluid streamlines become more evenly spaced in the exit far from the pinch, causing the particle exit positions to become closer to the upper wall.

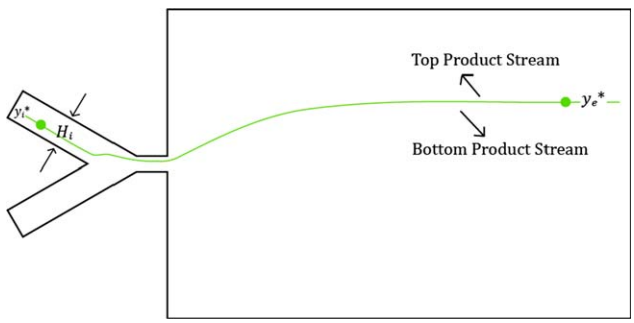

Figure 17. Separation trajectory of a particle entering the inlet at position y_i^* and proceeding to the exit at position y_e^*, which separates the top and bottom product streams.

[Color figure can be viewed in the online issue, which is available at wileyonlinelibrary.com.]

Concluding Remarks

This work provides theoretical and experimental studies of particle transport in a microfluidic device at low Reynolds numbers. The effects of systematically changing channel geometry and flow ratios on the trajectories were investigated for particles of different sizes being transported through a PFF device. The ability to predict particle trajectories through complex channel geometries such as a PFF device, and to determine how these trajectories deviate from fluid streamlines, aids in the design of devices with higher particle separation efficiency.

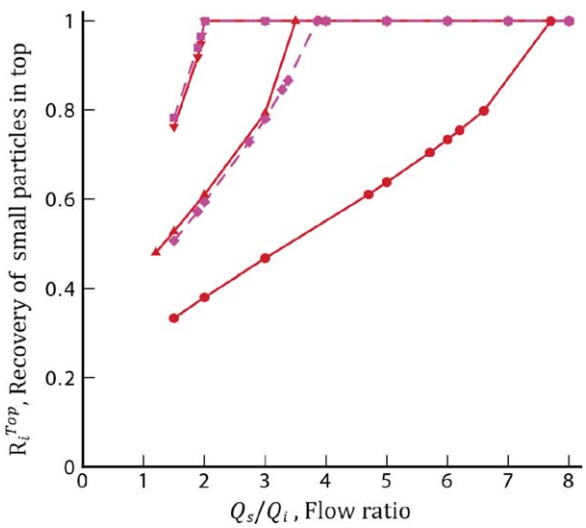

Figure 18. Recovery of smaller particles in the top outlet as a function of flow ratio, for several pairs of small and larger particles with η_i, $\eta_j = 0.2$, 0.4 (▼), 0.2, 0.6 (▲), 0.2, 0.8 (◇), 0.4, 0.6 (■), and 0.4, 0.8 (◆).

[Color figure can be viewed in the online issue, which is available at wileyonlinelibrary.com]

Table 3. Comparisons of Experimental Results to BIM Simulations for Particle Lateral Exit Positions at Varying Lateral Entry Positions and Flow Ratios

η	Q_s/Q_i	P	$2(y/H)_{sim}$	$2(y/H)_{exp}$
0.25	2	0.1	0.27	0.26
0.25	2	0.5	0.45	0.44
0.25	2	0.9	0.68	0.71
0.25	8	0.5	0.61	0.59
0.25	35	0.1	0.76	0.74
0.25	35	0.5	0.76	0.74
0.5	4	0.1	0.41	0.44
0.5	4	0.5	0.49	0.50
0.5	4	0.9	0.49	0.50
0.5	9	0.5	0.49	0.50
0.5	35	0.1	0.49	0.50
0.5	35	0.5	0.49	0.50

Here, y_e is measured from the channel midplane, and so $2y_e/H_e = 1.0$ is at the top wall of the exit. The longitudinal position at which the comparison is made is $x_e/L_e = 0.98$. The volumetric flow rate in the sweep stream was $Q_s = 5$ mL/min for all experiments in this table.

A moving-frame, boundary-integral method (MFBIM) for handling particles that approach or even touch the channel walls and corners was implemented, resulting in the reduction of computational resources. A critical flow ratio of the sweep and particle inlet streams, $(Q_s/Q_i)_c$, where all particles (for a given particle diameter of 20–80% of the pinch height) reach the upper wall of the pinch and depart on the same downstream trajectory, was determined. A minimum separation flow ratio $(Q_s/Q_i)_s$, where complete separation of two particle sizes occur, was also determined. The values of $(Q_s/Q_i)_c$ and $(Q_s/Q_i)_s$ were found to decrease with an increase in the size of the larger particle. In particular, $(Q_s/Q_i)_c$ decreases from 32 for $\eta = 0.2$ to 2.7 for $\eta = 0.8$, and $(Q_s/Q_i)_s$ decreases from 13 to 2.1 when the larger particle size is increased from $\eta_j = 0.3$ to $\eta_j = 0.8$, with a smaller particle size of $\eta_i = 0.2$ (this minimum separation ratio was found to be nearly independent of the size of the smaller particle). The ability to predict the separation flow ratios provides a means to quantify separation efficiency, and was used to design a PFF device having greater particle separation efficiency.

A channel geometry that delivers the greatest particle separation based on the lowest overall flow ratio can be predicted based on our MFBIM simulations. Variations to the inlet, pinch, and outlet areas of the PFF geometry were examined to determine the effects of channel geometry on particle trajectories and separation efficiency. Of the geometries simulated using MFBIM, the base case configuration with a square exit provides the maximum particle separation with the lowest flow ratio of the sweep and inlet channels. An angled exit from the pinch region has reduced separation efficiency, due to particle–wall interactions, as does a beveled exit. Changing the inlet geometry or pinch length had essentially no effect, as the flow is fully developed before reaching the pinch exit.

Experiments were conducted to test and validate our model using a PFF device. The device was fabricated using the channel geometry with greatest separation efficiency predicted by MFBIM simulations. Lateral exit positions and trajectories were obtained experimentally using small and large ($\eta = 0.25,\ 0.5$) polystyrene particles. The particles were tracked using subcritical and supercritical flow ratios obtained from simulations. Variation in lateral exit positions at subcritical flow ratios were greater, as expected, than those from supercritical flow ratios, due to the fact that subcritical flow ratios give rise to "banding" effects. At supercritical flow ratios, a single trajectory was observed, with minimal variation in lateral exit position for both particle sizes. To experimentally examine the effect of lateral particle entry position on lateral exit position, particles were tracked at subcritical flow ratios.

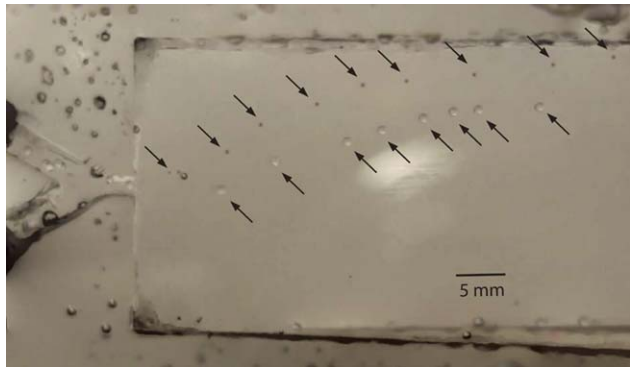

Figure 19. Time-lapse photographs of experiments (particle positions shown by arrows) for a supercritical flow ratio of $Q_s/Q_i = 35.0$, with Q_i, $Q_s = 0.14$, 5 mL/min (respectively).

The two particle sizes shown are: $\eta = 0.25$ (downward-facing arrows) and $\eta = 0.5$ (upward-facing arrows). [Color figure can be viewed in the online issue, which is available at wileyonlinelibrary.com.]

Comparisons of values obtained from simulation and experimentation show qualitative agreement for predicted lateral exit positions, with the smaller particles exiting on higher trajectories, as expected. However, differences are observed in the particle trajectories predicted by the MFBIM and those obtained experimentally. We believe that the discrepancy between theory and experiment is due to inertial effects and the small aspect ratio of the exit area. Unfortunately, it was not feasible to operate the device with such low flow rates that Re $<<$ 1 was achieved, because the long transit times then allowed the particles to approach the horizontal walls due to imperfect density match of the particles and fluid.

Acknowledgment

The authors thank the Ashley/McCormick Research Institute (06204591) for funding.

Literature Cited

1. Khan S, Gunther A, Schmidt M, Jensen K. Microfluidic synthesis of colloidal silica. *Langmuir*. 2004;20:8604–8611.
2. Nisisako T, Torii T, Higuchi T. Novel microreactors for functional polymer beads. *Chem Eng J*. 2004;101:23–29.
3. Sugiura S, Nakajima M, Ito H, Seki M. Synthesis of polymeric microspheres with narrow size distributions employing microchannel emulsification. *Macromol Rapid Commun*. 2001;22:773–777.
4. Larsen V, Poulsen L. Birgens H, Dufva M, Kristensen A. Pinched flow fractionation devices for detection of single nucleotide polymorphisms. *Lab Chip*. 2008;8:818–821.
5. Maenaka H, Yamada M, Yasuda M, Seki M. Continuous and size-dependent sorting of emulsion droplets using microfluidic hydrodynamics in pinched microchannels *Langmuir*. 2008;24:4405–4410.
6. Inglis D, Davis J, Zieziulewicz T, Lawrence D, Austin R, Sturm J. Determining blood cell size using microfluidic hydrodynamics. *J Immunol Methods*. 2008;329:151–156.

7. Matsuda M, Yamada M, Seki M. Blood cell classification utilizing hydrodynamic filtration. *Electron Commun Jpn*. 2011;94:1–6.
8. Gawad S, Schild L, Renaud, P. Micromachined impedance spectroscopy flow cytometer for cell analysis and particle sizing. *Lab Chip*. 2001;1:76–92.
9. Li H, Bashir R. Dielectrophoretic separation and manipulation of live and heat-treated cells of Listeria on microfabricated devices with interdigitated electrodes. *Sens Actuators B*. 2002;86:215–221.
10. Tsutsui H, Ho C. Cell separation by non-inertial force fields in microfluidic systems. *Mech Res Commun*. 2009;36:92–103.
11. Kersaudy-Kerhoas M, Dhariwal R, Desmulliez M. Recent advances in microparticle continuous separation. *IET Nanobiol*. 2008;2:1–13.
12. Blom M, Chmela E, Gardeniers J, Tijssen R, Elwenspoek M, Van den Berg A. Design and fabrication of a hydrodynamic chromatography chip. *Sens Actuators B*. 2002;82:6761–6768.
13. Chmela E, Tijssen R, Blom M, Gardeniers J, Van den Berg A. A chip system for size separation of macromolecules and particles by hydrodynamic chromatography. *Anal Chem*. 2002;74:3470–3475.
14. Edwards T, Gale B, Frazier A. A microfabricated thermal field-flow fractionation system. *Anal Chem*. 2002;74:1211–1216.
15. Janca J, Berneron J, Boutin R. Micro-thermal field-flow fractionation: new high-performance method for particle size distribution analysis. *J Colloid Interface Sci*. 2003;260:317–323.
16. Nilsson A, Petersson F, Jonsson H, Laurell T. Acoustic control of suspended particles in micro fluidic chips. *Lab Chip*. 2004;4:131–135.
17. Yamada M, Kasim V, Nakashima M, Edahiro J, Seki M. Continuous cell partitioning using an aqueous two-phase flow system in microfluidic devices. *Biotechnol Bioeng*. 2004;88:484–489.
18. Giddings J. A system based on split-flow lateral-transport thin (SPLITT) separation cells for rapid and continuous particle fractionation. *Sep Sci Technol*. 1985;20:749–768.
19. Jiang Y, Kummerow A, Hansen M. Preparative particle separation by continuous SPLITT fractionation. *J Microcolumn Sep*. 1997;9:261–273.
20. Fuh D. Peer reviewed: split-flow thin fractionation. *Anal Chem*. 2000;72:266A–271A.
21. Nakashima M. Pinched-flow fractionation (PFF) for continuous particle separation in microfluidic device, In: 17th IEEE International Conference on Micro Electro Mechanical Systems, Taipei, Taiwan, January 25–29, 2004;33–36.
22. Yamada M, Nakashima M, Seki M. Pinched flow fractionation: Continuous size separation of particles utilizing a laminar flow profile in a pinched microchannel. *Anal Chem*. 2004;76:5465–5471.
23. Kim W, Park Y, Shin J, Lee D. Size determination of diesel soot particles using flow and sedimentation field-flow fractionation. *Anal Chem*. 1999;71:3265–3272.
24. Moon M, Kim H, Kwon S, Lee S, Chang Y, Lim H. Pinched inlet split flow thin fractionation for continuous particle fractionation: application to marine sediments for size-dependent analysis of PCDD/Fs and metals. *Anal Chem*. 2004;76:3236–3243.
25. Takagi J, Yamada M, Yasuda M, Seki M. Continuous particle separation in a microchannel having asymmetrically arranged multiple branches. *Lab Chip*. 2005;5:778–784.
26. Andersen K, Levinsen S, Svendsen W, Okkels F. A generalized theoretical model for continuous particle separation in a microchannel having asymmetrically arranged multiple branches. *Lab Chip*. 2009;9:1638–1639.
27. Bruus H. Theoretical Microfluidics, 1st ed. Cary, NC: Oxford University Press, 2007.
28. Zinchenko A, Ashley J, Davis R. A moving-frame boundary-integral method for particle transport in microchannels of complex shape. *Phys Fluids*. 2012;24:043302.
29. Pozrikidis C. Boundary-integral and Singularity Methods for Linearized Viscous Flow. Cambridge, UK: Cambridge University Press, 1992.
30. Ladyzhenskaya O. The Mathematical Theory of Viscous Incompressible Flow (revised 2nd ed.). New York: Gordon and Breach Science Publishers, 1969.
31. Kim S, Karilla S. Microhydrodynamics–Principles and Selected Applications. Mineola, NY: Dover, 2005.
32. Haraldsson K, Hutchison J, Anseth K, Bowman C. 3D polymeric microfluidic device fabrication via contact liquid photolithographic polymerization (CLiPP). *Sens Actuators B*. 2006;113:454–460.
33. Hutchison J, Haraldsson K, Good B, Sebra R, Luo L, Anseth K, Bowman C. Robust polymer microfluidic device fabrication via contact liquid photolithographic polymerization (CLiPP). *Lab Chip*. 2004;4:658–662.
34. Ashley J, Cramer N, Davis R, Bowman C. Soft-lithograpy fabrication of microfluidic features using thiol-ene formulations. *Lab Chip*. 2011;11:2772–2778.

Manuscript received Dec. 12, 2012, and final revision received Mar. 2, 2013.